Hindawi
Structural Control and Health Monitoring
Volume 2024, Article ID 6153935, 18 pages
https://doi.org/10.1155/2024/6153935

WILEY | Hindawi

Research Article

A Baseline-Free Electromechanical Impedance Resonance Method for Measuring the Modulus of Elasticity of Concrete Cubes Using Surface-Bonded PZT Patches

Xiong Sha and Songye Zhu

Department of Civil and Environmental Engineering, The Hong Kong Polytechnic University, Hong Kong, China

Correspondence should be addressed to Songye Zhu; songye.zhu@polyu.edu.hk

Received 5 April 2023; Revised 7 July 2023; Accepted 11 January 2024; Published 25 January 2024

Academic Editor: Łukasz Jankowski

The modulus of elasticity of concrete (E_c) is an essential parameter commonly used in concrete design, concrete curing monitoring, and deterioration evaluation and damage detection of concrete structures. A quick and reliable *in situ* determination of E_c helps in accurate decision-making for construction and maintenance. The electromechanical impedance (EMI) technique using surface-bonded lead zirconate titanate (PZT) patches (referred to as SBP) has become a popular nondestructive method for monitoring concrete structures due to ease of operations. The existing research mainly utilized baseline-dependent approaches to monitor the changes (e.g., hardening or damage evolution) of concrete structures. However, relevant baselines are greatly influenced by the status of PZT sensors and bonding layers, limiting the practical applications of this technique. This paper presents a baseline-free EMI resonance method for measuring E_c of concrete without using prior baseline data for the first time. Numerical and experimental studies on standard concrete cubes (100 mm in width) with SBP were conducted to examine the proposed method. A dimensionless physical quantity was first proposed to view the EMI signals. Then, resonance peaks highly related to concrete properties but insensitive to the status of the sensor system were selected, physically described, and correlated to the concrete parameters through numerical analyses. Finally, experimental validations, covering the measurement of E_c, repeatability of the chosen resonance peaks, and temperature effects, were conducted to illustrate the proposed method's stability, accuracy, and sensitivity.

1. Introduction

Concrete is a composite material composed of multiple constituent materials. Two essential material properties, namely, compressive strength and modulus of elasticity, are inevitably used in the design of concrete structures. These two properties are highly related to concrete mix design, handling, compaction, and curing conditions [1]. Compressive strength (f_c') and modulus of elasticity (E_c) are usually obtained from destructive tests of standard concrete specimens in the laboratory [2]. In practice, E_c is often indirectly estimated from f_c' because the destructive tests for E_c are labor-intensive and time-consuming. For example, ACI-318-19 [3] provides two equations to estimate E_c based on f_c' with or without considering density ρ_c. Given that at least three specimens are needed to obtain stable results in such destructive tests, many specimens need to be prepared in long-term tests to obtain the properties at different ages of interest.

Various nondestructive testing techniques, such as ultrasonic pulse velocity measurements [4] and resonant frequency tests [5], have been proposed to estimate E_c of concrete and monitor concrete structures. Piezoelectric materials have been widely applied to monitor metallic, concrete, and composite structures [6–8] by employing two common techniques, namely, electromechanical impedance (EMI) and wave propagation technique [8]. The EMI technique proposed by Liang et al. [9] has been gradually considered an effective tool for monitoring concrete properties, in which the mechanical impedance of a host

structure is coupled with the electric impedance of a lead zirconate titanate (PZT) sensor, and thus, the coupled EMI can be obtained and analyzed easily. Compared with other nondestructive methods, the EMI technique has numerous advantages, including low cost, ease of installation, and convenience of testing (only one sensor and one device are needed) [10]. Piezoelectric materials (e.g., PZT) are typically employed as sensors in EMI techniques.

In EMI-based concrete monitoring, piezoelectric materials can be directly bonded on concrete surfaces, embedded inside the concrete, or indirectly installed on a concrete structure through an agent [10, 11]. Surface-bonded PZT (SBP) transducers refer to PZT sensors directly bonded to host structures using adhesive materials, and they have been proven effective in monitoring the strength development of cementitious-based materials through the EMI technique. Concrete cubes [12, 13] and cylinders [14–16] were monitored during their curing age. In those investigations, the PZT sensors were mounted to the concrete surface after demolding. The changes in the resonance peaks of the PZT and structural resonance peaks (e.g., cubes) obtained by the SBP were correlated to the development of the strength or modulus of elasticity of concrete [12–16].

Monitoring concrete using the EMI technique was first conducted by Soh and Bhalla [12], wherein they took the first PZT resonance peak as an indicator of concrete strength development. The results showed that the first PZT resonance peak (distinct in conductance spectra) effectively indicated that the peak shifts rightward and downward with the curing occurrence and increasing curing age. Compared with other resonance peaks of a PZT patch, the first resonance peak, which depends on the size of the PZT patch, appears at relatively low frequencies (typically between 80 kHz and 200 kHz) and is less sensitive to the variation in bonding conditions [17–19]. Therefore, most of the existing studies used the first PZT resonance peak (e.g., the changes in its magnitude and frequency) to monitor the concrete curing process [10]. Other important features that can be extracted from obtained signals are structural resonance peaks, which are considered to reflect the status of a host structure or specimen. The frequency upper bound of structural resonance peaks is often smaller than the frequency range of the first PZT resonance peak [10]. Statistical models, e.g., root mean square deviation (RMSD), are frequently used to evaluate the changes in the structural resonance peaks during concrete hardening and damage tests. Machine learning was also introduced to improve the ability of these statistical models to monitor structural changes autonomously [20].

Notably, baseline signals, which are typically measured in initial conditions, are vital for evaluating results when the abovementioned methods are applied. However, the baseline characteristics are highly sensitive to the status of the sensor system (i.e., the PZT sensor and the bonding layer), leading to limited generalizability for this technique. For instance, the mechanical properties of the piezoelectric material and the sensor's dimension have noticeable effects on the frequency of the first resonance peaks. Meanwhile, Yang et al. [17, 18] investigated the effect of the bonding layer thickness in the EMI technique. The results showed that a bonding layer thicker than 1/3 of the PZT patch thickness adversely affected monitoring, particularly in the high-frequency range (>100 kHz). The first PZT resonance peak shifted leftward with the increase of the thickness of the bonding layer. Similar observations were reported by Qing et al. [19]. Shin et al. [14] found that the initial bonding conditions can have a considerable influence on the obtained baseline for the statistical index-based approach. Moreover, the length of electric wires also affected the PZT resonance peaks [21]. Hence, generalized analytical models are not easy to be derived for the baseline-dependent approaches.

Temperature influences on the sensor system have been regarded as another important issue for baseline-dependent approaches in the EMI technique [22, 23] and make the analyses difficult. Bonding material properties can be varied easily by temperature changes [17]. For instance, the modulus of elasticity of the bonding material decreases considerably at high temperatures, resulting in apparent signal movement. Moreover, the dielectric, mechanical, and piezoelectric properties of piezoelectric materials vary with respect to changes in temperature, wherein the dielectric constants and piezoelectric coupling constants are the most sensitive, leading to variations in the frequency and amplitude of the resonant modes of the PZT patch [24]. The thermal-dependency parameters have different changing ratios for different types of piezoelectric materials. For example, type PZT-5H has very different thermal behaviors from type PZT-5A [25]. Therefore, complex compensation strategies should be made for different piezoelectric materials and adhesive materials in consideration of their individual temperature dependency.

In comparison, baseline-free methods of the EMI techniques using the frequency shift of structural resonance peaks were developed recently for different materials. Tang et al. [26] and Lu et al. [27] presented a baseline-free method to predict the modulus of elasticity of adhesive materials and cementitious materials, respectively. Frequency changes in the selected structural peaks are linearly correlated with the modulus of elasticity. Prim-type specimens in small sizes were employed and studied experimentally and numerically. The results showed the promising application of the EMI technique in predicting the physical parameters of a host structure. However, the small prim-type specimens cannot be used for concrete materials because aggregates cannot be included. *In situ* concrete monitoring is hard to be performed using such nonstandard specimens on real construction sites. Kong and Lu [28] found that the EMI technique could capture the natural frequencies of resonant modes of concrete cylinders and named it the EMI resonance method. The first two longitudinal modes captured by the embedded PZT sensor were employed to evaluate the modulus of elasticity of concrete cylinders, and the results showed a good agreement with that obtained from the traditional vibration-based testing method. However, the embedded PZT sensors should be carefully fabricated and installed, which may limit its application scenarios.

The abovementioned research concludes that the baseline-dependent approaches are highly sensitive to the

status of the sensor system, leading to the inconvenient and complex implementations of the EMI techniques. Meanwhile, a baseline-free method utilizing the resonance of a host structure (e.g., the EMI resonance method) has promising application scenarios in concrete structures. The following research gaps can be identified in the existing studies: (1) Reproducible characteristics of the signals (i.e., resonant frequencies of cubes) that are highly related to the properties of concrete cubes and insensitive to the status of the sensor system are needed. (2) The physical meanings of resonance peaks for specific host structures (e.g., standard cubes commonly tested in the field of concrete materials) need to be understood to achieve quantitative evaluation. (3) A quick and convenient assessment employing the selected characteristics is needed for concrete monitoring, which has the potential to be extended to different types of concrete structures.

To this end, this study presents the first baseline-free framework for measuring the modulus of elasticity of concrete using the EMI resonance technique and concrete cubes with SBP. Standard concrete cubes with SBP are investigated numerically and experimentally to bridge the abovementioned gaps, thereby shedding light on future research on the monitoring of concrete curing, degradation, and damage. The rest of this paper is organized as follows: Reproducible features in the EMI spectra of concrete cubes installed with different sizes of SBP are discussed and extracted through a numerical model first. Then, the stability of the extracted features is analyzed by considering the effects of dimensions and thermal effects on PZT patches and bonding layers. The correlations between the concrete material properties and selected features are established. Finally, the measurement accuracy, signal repeatability, and temperature effects are investigated and validated experimentally.

2. Numerical Investigations on Suitable EMI Indicators

2.1. Numerical Simulation Setup. Although 1-D and 2-D interactions between a PZT transducer and a host structure have been derived previously [9, 29, 30], similar derivation in 3-D structures is challenging. The finite element method (FEM) can simplify the analyses of such 3-D problems. In comparison, conventional analytical models can hardly accurately investigate the bonding layer effects. Therefore, FEM is an effective tool for simulating dynamic interactions in EMI techniques [24, 26, 31, 32]. A commercial FEM software, ANSYS, is used in the present study for multiphysics harmonic analysis in the coupled electromechanical field. The detailed principle for the piezoelectric analysis in ANSYS can be found in the studies by Yang et al. [17, 18] and Ai et al. [24].

A standard concrete cube (100 mm in width), widely used in concrete-related codes, is simulated as a host specimen whose modulus of elasticity is to be measured. In practical laboratory tests, cubes can provide at least four surfaces for the sensor bonding, facilitating the validation of test repeatability. A square-section PZT patch is bonded to the surface center by using an adhesive material. The shape of the adhesive material is assumed as a cuboid with its width equal to that of the PZT patch. Taking advantage of the model symmetry, only a quarter model is numerically simulated to save computation time, as shown in Figure 1. Solid 5, a coupled field solid element with eight nodes, is used to model the PZT patch. Solid 45 is used for adhesive and concrete materials. The mechanical and piezoelectric properties of the PZT materials used in this study are listed in Table 1, which were given by the factory of the PZT patches. The material properties of the epoxy and concrete are listed in Table 2, which are consistent with those measured in the experimental section. The interface between the PZT layer and the adhesive layer is assumed to be fully bonded. The top surface of the concrete layer is selected as the target area by using target 170 element. The bottom surface of the adhesive layer is set as the contact area by using the contact 174 element. The PZT patch is excited by a sinusoidal voltage of 1 V in the polarization directions (i.e., between the top and bottom surfaces) within a wide frequency range of 0.5–250 kHz (step size: 0.5 kHz) to obtain the EMI signatures. After a convergence analysis of element sizes, an element mesh size of 0.05 mm is selected for the PZT and adhesive materials, and a mesh size of 1.25 mm is selected for the concrete, both satisfying the relationship between the element size and the minimum wavelength [32]. Free boundary conditions are employed in the models of the target samples [30], considering the concrete cubes were put on a table with low stiffness and friction in the experiments in Section 3.

In the literature, conductance (G) (i.e., the real part of the admittance) is often considered more sensitive to the changes of host structures (e.g., hardening and damage) than susceptance (B) (i.e., the imaginary part of the admittance). However, presenting G spectra only and neglecting the changes of the B spectra result in information loss. These two physical quantities obtained in the tests highly depend on the piezoelectric material properties. In practice, a dimensionless physical quantity is always preferred to improve the generalizability for piezoelectric materials of different properties. The phase, arctan (B/G), consisting of the conductance and susceptance, can provide promising evaluation results [33]. Since the B value is considerably larger than G, the shapes of the phase and conductance spectra tend to be mirror-symmetric, i.e., the peaks in the G spectra correspond to the valleys in the phase spectra. Therefore, the present study adopts a new physical quantity, i.e., arctan (G/B), which is the complementary angle of the phase. Its peak frequencies are consistent with those peaks in the conductance spectra. Signals obtained by the SBP of different dimensions are simulated and analyzed directly in the following sections.

2.2. Repeatable Signature for Different Sizes of PZT Patches. Although the EMI signals in a high-frequency range may be more sensitive to the changes in the status of the host concrete specimens (e.g., modulus of elasticity), they are also heavily affected by the PZT and epoxy dimensions [17]. It is

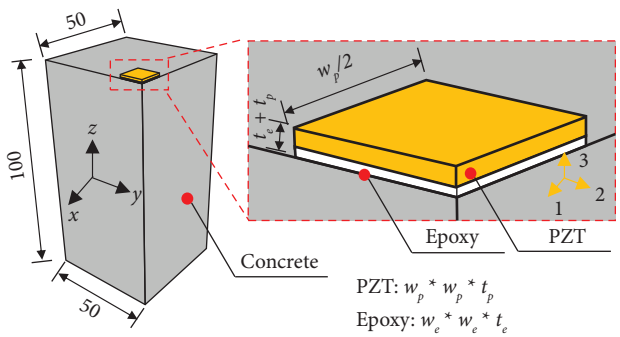

Figure 1: A quarter model adopted for simulations.

Table 1: Material properties of PZT used in simulations.

Parameters	Values
Relative permittivity $\boldsymbol{\varepsilon}^{\mathbf{S}}$ under constant strain (F/m)	$\varepsilon_{11}^{S} = \varepsilon_{22}^{S} = 1310$ $\varepsilon_{33}^{S} = 810$
Piezoelectric strain coefficients $\mathbf{d}$ (10^{-12} m/V)	$d_{31} = d_{32} = -255$ $d_{33} = 400$ $d_{52} = d_{61} = 650$
Compliance $\mathbf{s}^{\mathbf{E}}$ under short circuit (10^{-12} m^2/N)	$s_{11}^{E} = s_{22}^{E} = 16$ $s_{33}^{E} = 19$ $s_{12}^{E} = -5.13$ $s_{13}^{E} = s_{23}^{E} = -6.46$ $s_{44}^{E} = s_{55}^{E} = 45$ $s_{66}^{E} = 41$
Density, $\boldsymbol{\rho}_{\mathbf{p}}$ (kg/m^3)	7600
Dielectric loss factor, tan $\boldsymbol{\delta}$	0.02
Damping ratio, $\boldsymbol{\xi}_{\mathbf{p}}$	0.024

Table 2: Material properties of epoxy and concrete used in simulations.

Material	Parameters	Values
Epoxy	Density, $\boldsymbol{\rho}_{\mathbf{e}}$ (kg/m^3)	1100
	Modulus of elasticity, $\mathbf{E}_{\mathbf{e}}$ (GPa)	3.0
	Poisson's ratio, $\boldsymbol{\mu}_{\mathbf{e}}$	0.38
	Damping ratio, $\boldsymbol{\xi}_{\mathbf{e}}$	0.024
Concrete	Density, $\boldsymbol{\rho}_{\mathbf{c}}$ (kg/m^3)	2408
	Modulus of elasticity, $\mathbf{E}_{\mathbf{c}}$ (GPa)	30
	Poisson's ratio, $\boldsymbol{\mu}_{\mathbf{c}}$	0.20
	Damping ratio, $\boldsymbol{\xi}_{\mathbf{c}}$	0.008

a crucial task to search for signal characteristics that are sensitive to concrete property changes but insensitive to the properties of the PZT and adhesive materials.

Figure 2 shows signals' arctan (G/B) spectra in two frequency ranges, namely, 10–250 kHz and 10–70 kHz. Three different dimensions of PZT patches, $20 \times 20 \times 1.0$ mm^3, $10 \times 10 \times 1.0$ mm^3, and $10 \times 10 \times 0.5$ mm^3 (denoted as L-PZT, S-PZT, and ST-PZT, respectively), are simulated to consider two different widths and thicknesses of PZT patches. All these PZT patch sizes are frequently used and commercially available. The thickness of the adhesive layer is assumed to be 0.25 mm in this baseline case. As shown in Figure 2(a), the signals collected from the bonded PZT patches show that the dominant PZT resonance frequency in the arctan (G/B) spectra for L-PZT, S-PZT, and ST-PZT is 120, 192.5, and 220 kHz, respectively, indicating that the PZT patch with thin thickness and small width is associated with a high frequency of the first PZT resonant mode. From this perspective, the first PZT resonance frequency cannot be used directly to evaluate the changes in concrete cubes, if the PZT patches cannot be standardized in practical applications. Different dimensions of PZT patches should be analyzed separately, with varying material properties being considered simultaneously. In comparison, Figure 2(b) plots the signal spectra from 10 to 70 kHz, mainly including the cube resonance peaks of the host structure [10, 26, 27]. Almost the same peak frequencies can be obtained by different sizes of the PZT patches but in different magnitudes, as shown in Figure 2(b). It should be noted that Figure 2(b) shows double y axes since the magnitude of these curves differ significantly. The curves of ST-PZT and S-PZT correspond to left y-axis, while the curve of L-PZT corresponds to the right y-axis.

The sensitivity with respect to the size of the PZT patch can be evaluated by comparing the peak amplitudes. The spectra obtained by the L-PZT show larger responses than the other two small PZT patches on the standard concrete cubes. The sensitivity of the thin ST-PZT is slightly higher than that of the thick one (S-PZT). For instance, the magnitude of peak A is around 0.1 (from 1.0 to 1.1) obtained by ST-PZT and S-PZT and around 1.3 (from 1.5 to 2.8) obtained by L-PZT. Therefore, the sensitivity order to capture the cube resonance peaks in 10–70 kHz is L-PZT > S-PZT > ST-PZT. Despite the obviously different peak amplitudes, reproducible cube resonance peaks can be captured by different sizes of the PZT patches in 10–70 kHz.

2.3. Vibration Modes of Interested Peaks. Based on the abovementioned description, different vibration modes of the concrete cube can be excited and recorded by the PZT sensors with sweeping frequencies. This subsection discusses the behavior of the different peaks in different frequency ranges. Figure 3 shows the deformation of different vibration modes when the cube is excited by the S-PZT patch, wherein the vibration modes are classified into two groups, the PZT resonance peaks and cube resonance peaks in 100–250 kHz and the cube resonance peaks in 10–70 kHz. Each vibration mode corresponds to one peak labeled by a circle in Figure 2. Peaks 1–3 in Figure 3(a) show the main deformation concentrated in the field near the PZT sensor, implying that the frequency changes of the corresponding peaks highly depend on the PZT sensor property, adhesive layer, and nearby concrete.

In terms of the 15 peaks (i.e., peaks A to O) shown in Figure 3(b), the deformation is distributed in the entire concrete cube structure, which explains why they are referred to as cube resonance peaks. For example, peak A shows a bending mode, in which the top (the face bonded with the PZT sensor) and bottom surfaces bend in the same direction. The minimum displacement in blue color occurs at the middle center of the side surface, whereas the

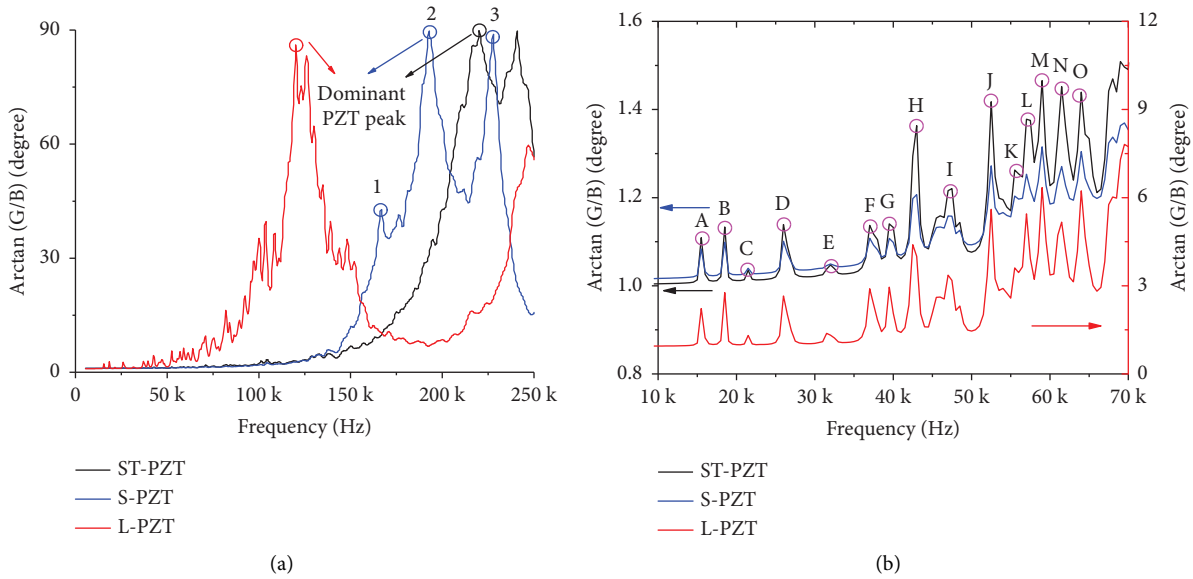

FIGURE 2: Effect of the PZT size on different frequency ranges. (a) 0–250 kHz. (b) 10–70 kHz. (Note: the subfigure (b) has double y axes, where the ST-PZT and S-PZT curves correspond to the left y axis, while the L-PZT curve corresponds to the right y axis).

maximum displacement in red color is observed at the corners in the same direction (along Z-axis). For peak B, the top and bottom surfaces bend in the opposite direction, with the minimum transformation observed at the middle point of the sideline. Peak C presents a breathing vibrating mode, in which the maximum displacements are seen on the corners of the top and bottom surfaces that are in the opposite trends. The signal spectra in Figure 2 show the peak C amplitude is much lower than those of other modes. At peak D, the side surfaces show shear deformation, and the vibration mode of the corners and the middle points of the sideline are in opposite directions. Peak E also has a weak response and cannot be observed directly in the signal of the S-PZT. Peaks I to H correspond to high-order vibration modes excited, wherein the main deformations occur at the top and bottom surfaces.

2.4. Repeatability of Signal Characteristics at Different Adhesive Layer's Thickness. Parametric analyses regarding the adhesive layer thickness t_e are presented in this subsection. Three values $t_e = 0.25$, 0.50, and 0.75 mm are considered, all of which can be implemented easily in practice. Figure 4 shows the effect of the adhesive layer thickness on the obtained signals. As shown in Figure 4(a), the first PZT resonance peak of all the SBP shifts leftward with the increases of t_e, which agrees with the observations by other researchers [18, 19]. Considering the adhesive layer thickness t_e can hardly be controlled accurately, the first PZT resonance peak cannot be practically applied in a baseline-free method.

In comparison, in 10–70 kHz, the signal baseline shifts upward with the increase of t_e. However, the frequencies of the cube resonance peaks are not affected, although the magnitude decreases with the increase of t_e. In the signal spectra obtained from S-PZT, the relatively weak peaks (e.g., peaks C and E) are hardly observed when a thick adhesive layer is used. The frequencies of the peaks larger than 45 kHz obtained by S-PZT with $t_e = 0.75$ mm are inconsistent with the other two working conditions, as shown in Figure 4(b). Some peaks in this frequency range (i.e., 45–75 kHz) disappear, whereas others shift leftward. Therefore, the epoxy thickness for the S-PZT patch is suggested not to exceed 0.5 mm, which is practically achievable. Although some peaks weaken or even disappear in the spectra of ST-PZT, the frequencies of those observable peaks do not change in the whole 10–70 kHz, as shown in Figure 4(c). For the L-PZT shown in Figure 4(d), similar phenomena can be observed. The peaks weaken with the increase of t_e, and only peak E becomes hard to catch. The peaks obtained by L-PZT show the slightest reduction in the peak magnitudes with the increase of the t_e, whereas the signals obtained by S-PZT are the most influenced.

The discussion above indicates that the effect of the adhesive thickness t_e in the frequency range of 10–70 kHz is quite smaller than that in the high-frequency range. The frequencies of the first several peaks (peaks A to H) are maintained nearly constant given the dimensional changes of epoxy. In the following numerical parts, S-PZT is set as the default PZT patch, and 0.25 mm is used for t_e.

2.5. Repeatability of Signal Characteristics at Different Temperatures. Temperature influences both the mechanical properties of the adhesive materials and the mechanical and piezoelectric properties of the PZT materials, thereby leading to the changes in the frequencies of the resonance peaks of the PZT patches. Table 3 summarizes the temperature dependence of the material coefficients of PZT materials [34] and typical adhesive materials [24].

The temperature effect on the PZT and adhesive materials causes considerable changes in the signals that are highly related to the adhesive and PZT materials. However,

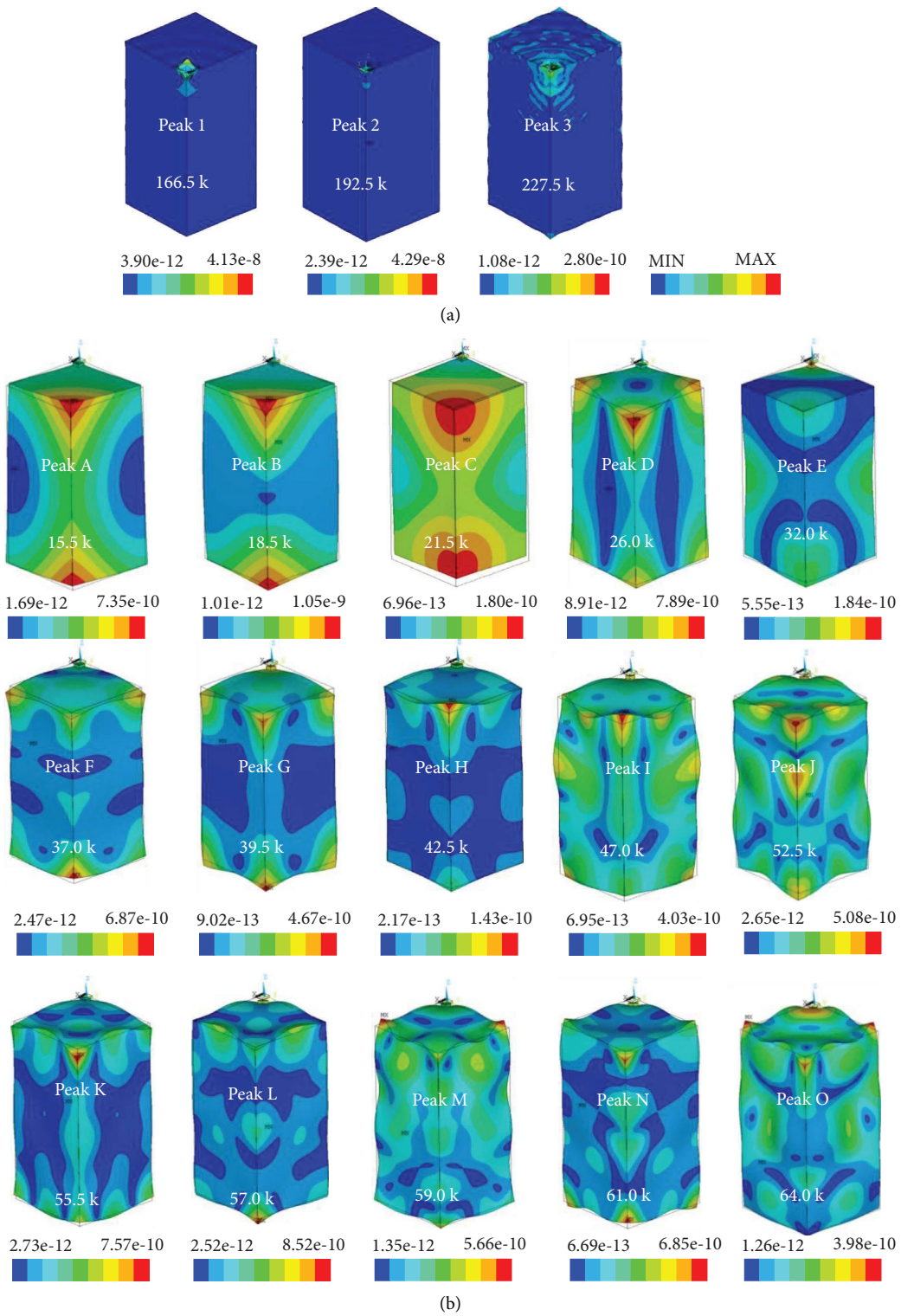

Figure 3: Summary of vibration modes. (a) Vibration modes of distinct cube and PZT resonance peaks. (b) Vibration modes corresponding to cube resonance peaks in 10–70 kHz.

the changes in signal characteristics corresponding to the properties of the host structures should be minimal. Figure 5 shows the arctan (G/B) signal spectra concerning the changes in the temperature in two frequency ranges (0–250 kHz and 10–70 kHz). The properties at room temperature (RT) are regarded as the control group. The thermal effects are applied only to the PZT and adhesive materials, and thus, the properties of PZT materials and adhesive materials vary with the temperature, whereas the concrete properties are fixed. The parameters listed in

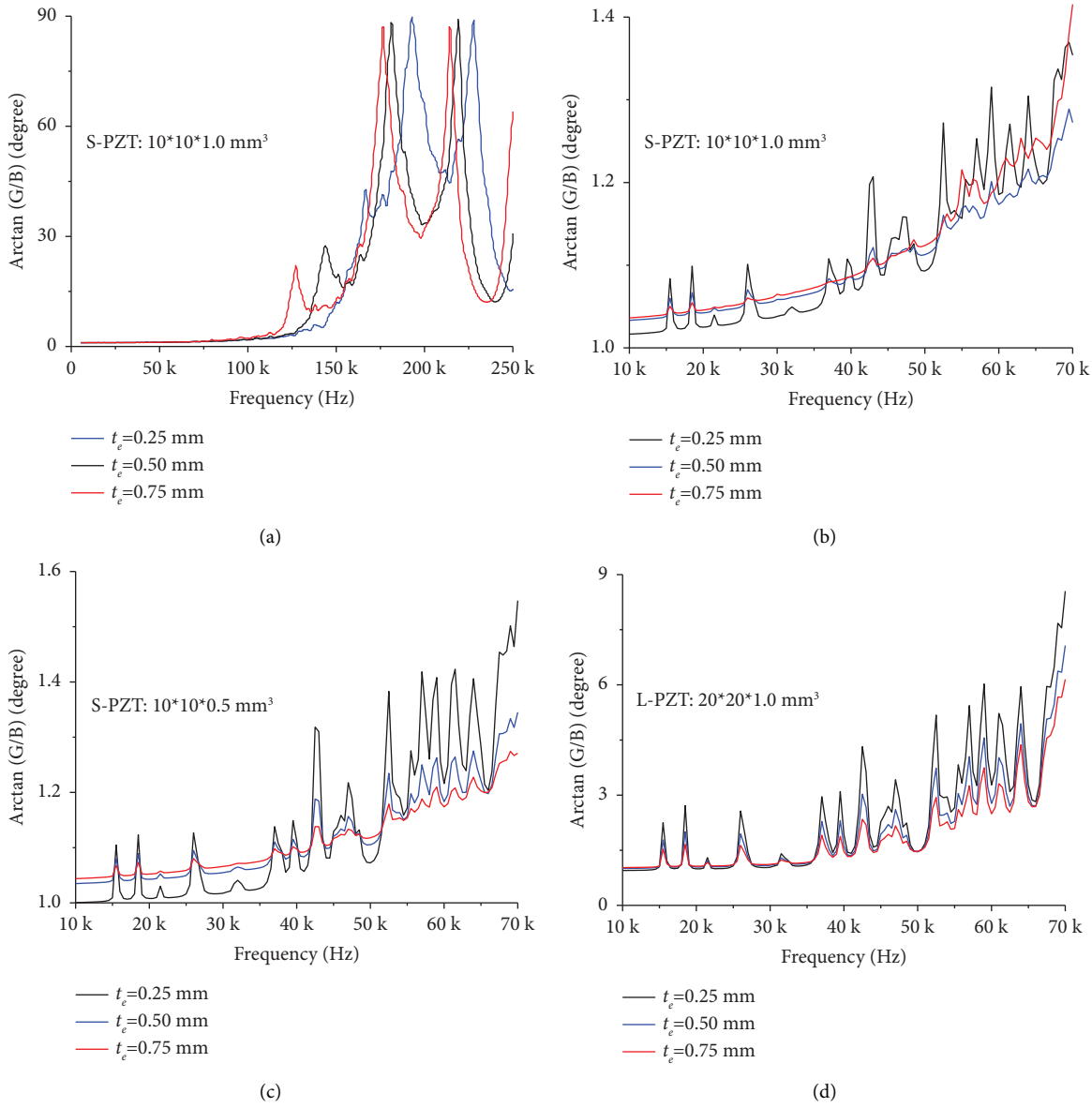

Figure 4: Effect of thickness of the adhesive layer on different frequency ranges. (a) 0–250 kHz of S-PZT. (b) 10–70 kHz of S-PZT. (c) 10–70 kHz of ST-PZT. (d) 10–70 kHz of L-PZT.

Table 3: Temperature dependence of material coefficients.

Material	Coefficient	Symbol	Rate (±15°C)
PZT	Piezoelectric strain coefficients	$\|d_{31}\|$	±6%
		d_{33}	±6%
		d_{15}	±1%
	Dielectric permittivity	ε_{11}	±10%
		ε_{33}	±3%
	Compliance coefficients	s_{11}	±1.5%
		$\|s_{12}\|$	±1.6%
		$\|s_{33}\|$	±0.8%
		$\|s_{55}\|$	±2.0%
Epoxy	Modulus of elasticity	E_e	±9%
	Poisson's ratio	μ_e	±0.02

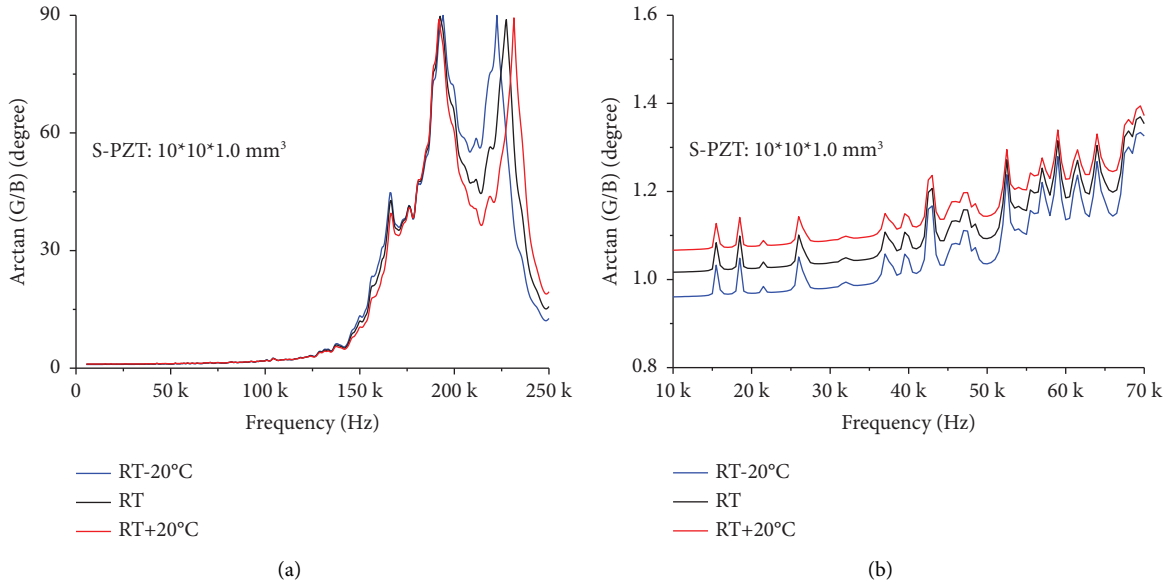

FIGURE 5: Temperature-induced changes in the PZT and adhesive materials. (a) 0–250 kHz of S-PZT. (b) 10–70 kHz of S-PZT.

Table 3 are used in the simulations. Figure 5(a) shows that the frequencies of the first PZT resonance peak vary with temperature changes, indicating that complex temperature-related modifications are needed to remove the temperature effect from the monitoring results.

In contrast, the interested signal spectra in 10–70 kHz shift upward with the temperature increase from RT – 20°C to RT + 20°C; however, no frequency changes of peaks occur, as shown in Figure 5(b). Therefore, the selected characteristics of the arctan (G/B) signal spectra in this frequency range are not affected by the thermal effects on the piezoelectric and adhesive materials. The changes in the adhesive layer (hardening or deterioration) will not lead to the frequency changes of the selected peaks, guaranteeing stability in a quick measurement and long-term monitoring.

2.6. Correlations between Signal Characteristics and Concrete Properties. The discussion above indicates that the frequencies of the peaks in 10–70 kHz are insensitive to the dimensional and thermal changes of the PZT and adhesive materials, particularly for the first several cube resonance peaks. In this subsection, the selected peaks are further investigated to build correlations with the properties of the concrete materials.

Zhou et al. [29, 35] and Zagrai et al. [29] derived a dynamic model for a bonded PZT actuator integrated with a 2-D structure (e.g., a thin plate) using the EMI technique. The theoretical formula implies that for different vibration modes (e.g., the in-plane and bending vibration modes), linear relationships exist between the modal frequencies and the square root of the modulus of elasticity of the structure divided by the density, i.e., $\sqrt{E/\rho}$, when Poisson's ratio and dimensions of the host structure are fixed. This study considers concrete after 28 days of curing age; thus, Poisson's ratio can be regarded as stable and is often set as 0.2 for concrete materials. Therefore, modulus of elasticity E_c and density ρ_c are two important parameters that determine the frequencies of different vibration modes of a concrete cube. In addition, the damping ratio of concrete materials, ξ_c, is also studied parametrically. The modulus of elasticity is set from 15 GPa to 55 GPa with an interval of 2.5 GPa. The density of the concrete varies from 2308 kg/m^3 to 2508 kg/m^3 with an interval of 100 kg/m^3. The damping ratio of the concrete cubes typically varies from 0.8% to 2.1% [24]; thus, three damping ratios (0.8%, 1.6%, and 2.4%) are considered in the parametric study.

Figure 6 shows the typical effects of the concrete properties on the interested frequency range. Only three spectra showing the effects of the modulus of the elasticity are plotted in Figure 6(a) for clarity. The frequencies corresponding to peaks A to D are summarized in Table 4. All the peaks shift rightward with the increases in the modulus of elasticity. In general, the peaks at higher frequencies shift larger horizontal distances. Similar trends can be observed in the effect of the density. All the peaks shift leftward with respect to the increases in density, as shown in Figure 6(b). In contrast, changes in the damping ratio in the selected range do not lead to any frequency changes in the selected peaks, as shown in Figure 6(c). But some peaks with small magnitude disappear or become difficult to be identified with the increases in the damping ratio (e.g., peaks C, E, and G).

The discussion above indicates that the frequencies of the selected peaks can be correlated to the values of E_c and ρ_c. The value of $\sqrt{E_c/\rho_c}$ (unit: m/s) is used to fit a linear relationship, as shown in the following equation:

$$f_i = \kappa_i \sqrt{\frac{E_c}{\rho_c}}, \tag{1}$$

where f_i (unit: Hz) is the frequency of the ith vibration mode and κ_i (unit: m^{-1}) refers to the slope for a specific vibration mode.

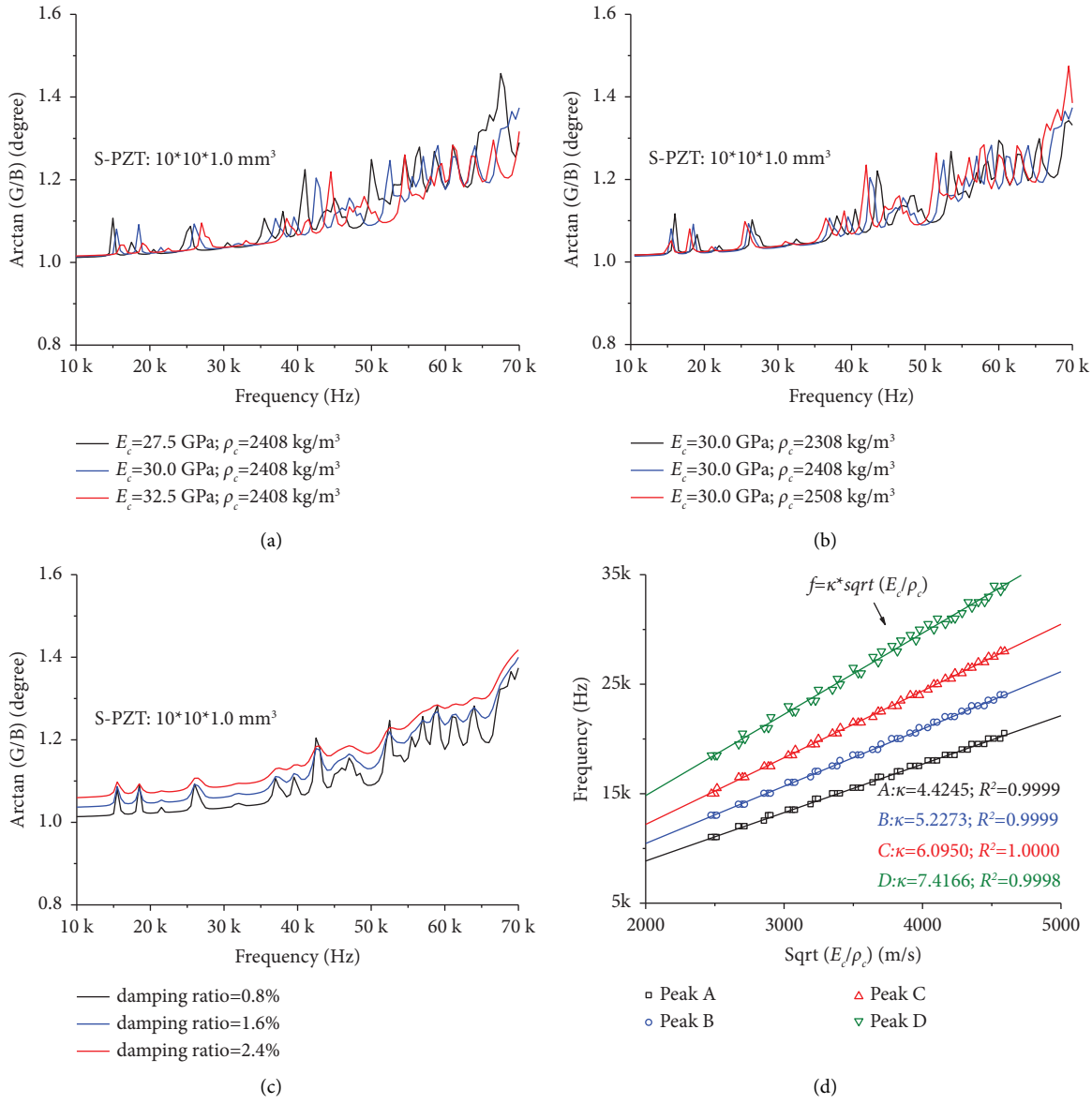

Figure 6: Effect of the properties of concrete material and regression results of the peaks. (a) Modulus of elasticity of concrete. (b) Density of concrete. (c) Damping ratio of concrete. (d) Regression analysis.

Table 4: Summary of the simulation results of peaks A to D.

E_c (GPa)	Frequency (kHz)											
	ρ_c = 2308 kg/m³				ρ_c = 2408 kg/m³				ρ_c = 2508 kg/m³			
	A	B	C	D	A	B	C	D	A	B	C	D
15.0	11.5	13.5	15.5	19.0	11.0	13.0	15.0	18.5	11.0	13.0	15.0	18.0
17.5	12.0	14.5	17.0	20.5	12.0	14.0	16.5	20.5	11.5	14.0	16.0	19.5
20.0	13.0	15.5	18.0	21.5	13.0	15.0	17.5	21.0	12.5	15.0	17.0	21.5
22.5	14.0	16.5	19.0	23.0	13.5	16.0	18.5	22.5	13.5	15.5	18.5	22.0
25.0	14.5	17.0	20.0	25.0	14.5	17.0	19.5	23.5	14.0	16.5	19.0	24.0
27.5	15.5	18.0	21.0	25.5	15.0	17.5	20.5	25.5	14.5	17.5	20.0	25.0
30.0	16.0	19.0	22.0	26.5	15.5	18.5	21.5	26.0	15.5	18.0	21.0	25.5
32.5	16.5	19.5	23.0	27.5	16.5	19.0	22.5	27.0	16.0	19.0	22.0	26.5
35.0	17.0	20.5	23.5	28.5	17.0	20.0	23.0	28.0	16.5	19.5	23.0	27.5
37.5	18.0	21.0	24.5	29.5	17.5	20.5	24.0	29.0	17.0	20.0	23.5	28.5

Table 4: Continued.

E_c (GPa)	Frequency (kHz) $\rho_c = 2308\ \text{kg/m}^3$				$\rho_c = 2408\ \text{kg/m}^3$				$\rho_c = 2508\ \text{kg/m}^3$			
	A	B	C	D	A	B	C	D	A	B	C	D
40.0	18.5	22.0	25.5	30.5	18.0	21.5	25.0	30.0	17.5	21.0	24.5	29.5
42.5	19.0	22.5	26.0	31.5	18.5	22.0	25.5	31.0	18.0	21.5	25.0	31.0
45.0	19.5	23.0	27.0	32.5	19.0	22.5	26.5	32.5	18.5	22.0	26.0	31.0
47.5	20.0	23.5	27.5	33.5	19.5	23.0	27.0	32.5	19.5	23.0	26.5	32.0
50.0	20.5	24.5	28.5	35.0	20.0	24.0	28.0	33.5	20.0	23.5	27.0	33.0
52.5	21.0	25.0	29.0	35.0	20.5	24.5	28.5	34.5	20.0	24.0	28.0	34.5
55.0	21.5	25.5	30.0	36.0	21.0	25.0	29.0	36.0	20.5	24.5	28.5	34.5

Figure 6(d) shows the regression results between $\sqrt{E_c/\rho_c}$ and the frequencies corresponding to cube resonance peaks A to D. The R^2 values show that the linear relationships fit the simulation results extremely well. Among these four peaks, peak D has the largest slope of 7.416 m^{-1}; the slopes of peaks A, B, and C are equal to 4.4245, 5.2273, and 6.0950 m^{-1}, respectively. In general, a higher-order vibration mode has a larger slope κ.

On the basis of these regression results, the modulus of elasticity of the concrete can be evaluated directly. After identifying the frequencies of the first four peaks from the arctan (G/B) spectra in the selected frequency range, $\sqrt{E_c/\rho_c}$ can be calculated. The density of concrete cubes is easy to be measured or estimated in practice. Consequently, the modulus of elasticity can be calculated on the basis of these peaks. Finally, the E_c values from different peaks can be averaged to reduce the errors caused by different vibration modes.

Therefore, the frequencies of the first several peaks in the arctan (G/B) spectra of the EMI signals in the frequency range of 10–70 kHz are suggested as the indexes to quantify the modulus of elasticity of concrete. The numerically obtained regression formulas shown in Figure 6(d) will be directly applied (without any modification) in the following experimental validations.

3. Experimental Validations

The experimental measurements of the moduli of elasticity of concrete cubes were conducted to validate the methods proposed in the last section and examine the repeatability of the proposed indexes in temperature effects.

3.1. Measurement of Modulus of Elasticity. Three batches of concrete cubes, using seawater sea-sand concrete (SSC) and high-strength concrete (HSC) with different densities and strengths, were cast to measure the moduli of elasticity. The corresponding material proportions of concrete are summarized in Table 5. Each batch contained three cubes (100 mm in width) and three cylinders (150 mm diameter and 300 mm height), where three cubes were used for the measurements using the proposed EMI method and three cylinders were for the conventional destructive compressive tests according to ASTM C39/C39M [2]. A minimum curing period of 28 days was implemented. For each concrete cube, a PZT patch with dimensions of $10 \times 10 \times 1.0\ \text{mm}^3$, corresponding to the S-PZT case in the FEM simulation, was bonded at the center point of the surface. Five-minute-fast epoxy (Devcon 14270) was used as the adhesive material. The thickness of the adhesive layer ranged approximately 0.10–0.35 mm, satisfying the requirement recommended above.

Figure 7 shows the test setup for the measurement. The EMI signal measurement system consisted of an LCR meter (keysight E4980AL) and a laptop for recording. EMI spectra were obtained by applying a voltage of 1 V across the terminals of the PZT patch over a frequency range of 0.5–250 kHz at 0.5 kHz intervals. The concrete cubes were placed on a wooden table with low stiffness and friction, whose boundary constraint effects are negligible according to the results of trial tests and simulations. The room temperature for measurement was around 20°C.

Meanwhile, conventional compressive tests were conducted to obtain the concrete strength f'_c. Three identical standard cylinders for each batch were tested according to ASTM C39/C39M [2]. The tests were performed by positioning the samples in a uniaxial loading device (340 tons). The average values of the compressive strength at 28-day curing age for batch I, batch II, and batch III were 46.1, 94.3, and 95.4 MPa, respectively; the corresponding coefficients of variation were 0.01, 0.02, and 0.03, respectively. The moduli of elasticity of these three different batches were subsequently estimated according to ACI-318 [3], as shown in the following equation:

$$E_c = 0.043\rho_c^{1.5}\sqrt{f'_c}\ \text{(in MPa)}. \tag{2}$$

Consequently, the E_c values were calculated as 33685, 50638, and 50931 MPa for batch I, batch II, and batch III, respectively, by substituting the corresponding value. The estimated moduli of elasticity were employed here, as the results can also be extended to correlate the strength of concrete and EMI signals. Although estimated indirectly, the modulus of elasticity determined using the above code equation, originally proposed by Pauw [36], has been proven acceptable for most applications over the past years [3]. For example, Vakhshouri [37] compared the estimation accuracies of the moduli of elasticity of concrete in 35 design codes and 19 empirical models and concluded that the code equation in ACI-318 [3] was relatively compatible with the randomly selected experimental results with a great variety

Table 5: Mix proportions of the tested concrete materials.

Batch	Material	Mix proportion by weight	Density (kg/m^3)	Curing days
I	SSC	C: SW: SS: CA: FA: PFA: SP[a] = 1 : 0.333 : 0.5 : 2.212 : 1.712 : 1.409 : 0.008	2370	28
II	HSC	C: W: S: CA: FA: SP[b] = 1 : 0.199 : 1.149 : 1.017 : 0.680 : 0.018	2450	28
III	HSC	C: W: S: CA: FA: SP = 1 : 0.199 : 1.149 : 1.017 : 0.680 : 0.018	2450	90

[a]C = cement; SW = seawater; SS = sea-sand; CA = 20 mm aggregate; FA = 10 mm aggregate; PFA = pulverized fuel ash. [b]W = water; S = sand.

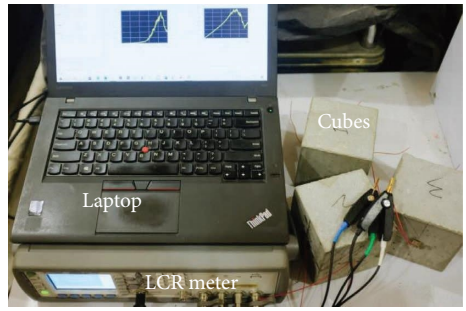

Figure 7: Test setup for measurement.

of aggregates, curing conditions, and testing methods and standards.

Figure 8 plots the experimental arctan (G/B) spectra obtained from the EMI tests of both batches. In the high-frequency range of 0.5–250 kHz, the first PZT resonance peak and the cube resonance peaks showed low repeatability in Figures 8(a) and 8(c), whereas reproducible signal spectra could be seen in the 10–70 kHz range, particularly for the first several peaks, as shown in Figures 8(b) and 8(d). The peaks at frequencies higher than 45 kHz showed relatively lower repeatability, but repeatable peaks from A to D could be observed in both batches, as shown in Figures 8(b) and 8(d). Peak C in batch I was not obvious; but in batch II, peak C could be identified easily.

Hence, only peaks A, B, and D that could be easily identified in the experimental results were selected to calculate the modulus of elasticity for each cube. The frequencies of the peaks were extracted first. Then, the moduli of elasticity were calculated using the regression relationships presented in Figure 6(d). The comparison of the compressive tests and SBP tests is shown in Figure 9 and summarized in Table 6. The largest error here was approximately −3.9%, which was small enough for concrete measurement. The mean errors for batch I and batch II were only −1.7% and −3.0%, respectively, proving that the proposed method is accurate in measuring the moduli of elasticity of concrete cubes. The proposed method could be extended to different sizes of concrete cubes or other concrete specimens by selecting suitable cube resonance peaks and calibrating the corresponding slopes κ.

Notably, the material properties obtained from low-strain nondestructive tests are sometimes called "dynamic" constants [38]. The complex relationships between "dynamic" and static moduli of elasticity remain ambiguous, as dynamic moduli of elasticity may depend on different resonant modes selected [5]. More experimental tests need to be conducted to clarify an accurate relationship, which is out of the major scope of this paper. Therefore, the estimated moduli of elasticity were directly compared with the static counterparts in this paper, given the relatively small differences between them.

The simulated signal spectra are also plotted in Figures 8(b) and 8(d) using the calculated results for each batch. Good agreements of frequencies could be observed in the peaks at a relatively low frequency (i.e., <40 kHz), which justifies the effectiveness of the major conclusions obtained in Section 2. At 40–70 kHz, however, the simulation results deviated from the experimental results. The differences might be attributed to the nonhomogeneous material properties of concrete that were not simulated in the FEM model. Real concrete materials consist of aggregates, sand, cement, and void, which involve complicated interfaces between different phases and affect the signals in a high-frequency range easily; however, the numerical model for concrete is assumed as homogenous in this study.

3.2. Repeatability Tests for Different Types of the Sensor System. Repeatable signal indexes are essential for the practical applications of EMI techniques. The numerical analyses in Section 2 indicated that the three selected sizes of PZT patches presented the same characteristic frequencies in the selected frequency range, but the signals obtained from L-PZT presented the highest sensitivity. Therefore, experiments using L-PZT and S-PZT were conducted to validate the results from numerical analyses. Three concrete cubes (batch III) were cast with the same material proportions of HSC and used for validation and further temperature tests. The tests were conducted after 90 days of curing age. For each concrete cube in batch III, an L-PZT ($20 \times 20 \times 1.0\,\text{mm}^3$) and an S-PZT ($10 \times 10 \times 1.0\,\text{mm}^3$) were bonded simultaneously to the opposite sides of the same cube by using a five-minute-fast epoxy (Devcon 14270), as shown in Figure 10(a). The thickness of the adhesive layers was around 0.2–0.3 mm. The signal from 10 to 70 kHz was measured with a small interval of 0.1 kHz to present clear movements of the signals.

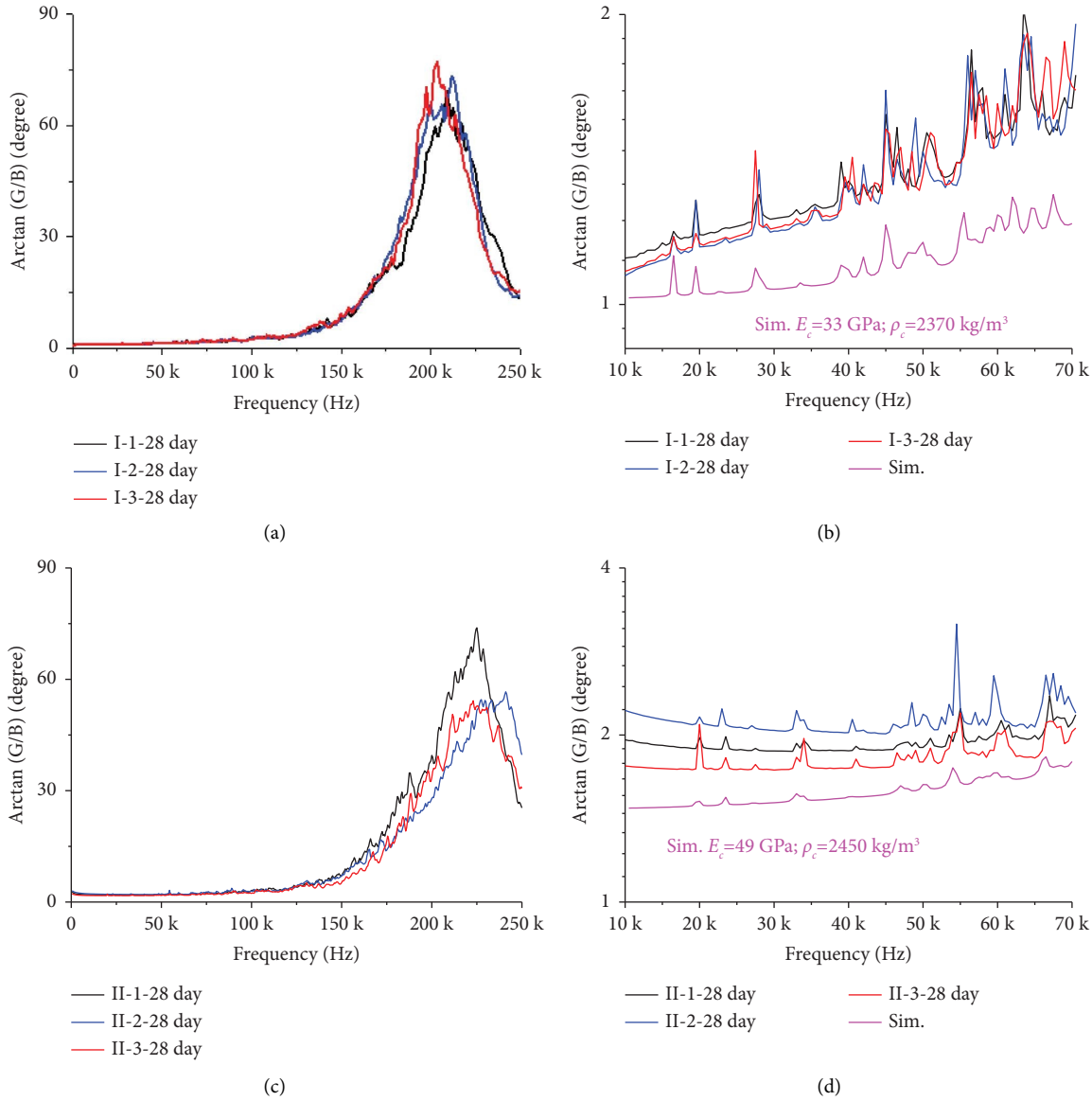

Figure 8: The measured arctan (G/B) spectra for two batches of concrete. (a) Batch I: 0.5–250 kHz. (b) Batch I: 10–70 kHz. (c) Batch II: 0.5–250 kHz. (d) Batch II: 10–70 kHz.

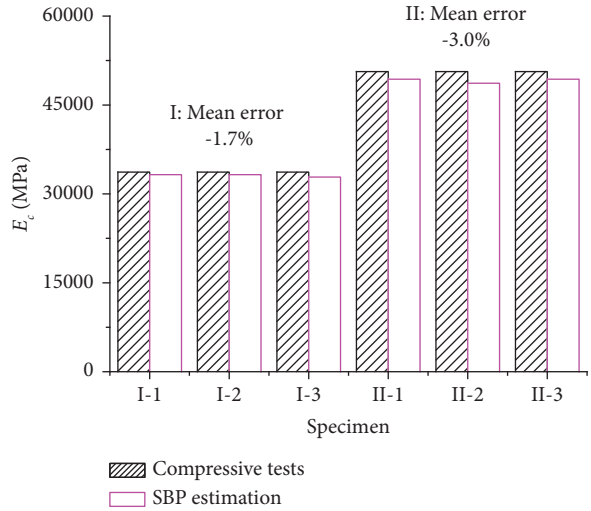

Figure 9: Comparisons between experimental results and predictions.

Table 6: Experimental results for E_c measurement.

Specimen†	Compressive test		SPB-based EMI test		Relative difference in E_c	
	f'_c (MPa)	E_c (MPa)#	Peaks A/B/D (kHz)	E_c (MPa)*	In (MPa)	In (%)
I-1	46.1 (0.01)^	33685	16.5/19.5/28.0	33240	445	−1.3
I-2			16.5/19.5/28.0	33240	445	−1.3
I-3			16.5/19.5/27.5	32842	843	−2.5
II-1	94.3 (0.02)	50638	20.0/23.5/33.0	49361	1277	−2.5
II-2			20.0/23.0/33.0	48666	1972	−3.9
II-3			20.0/23.5/33.0	49361	1277	−2.5

*Values are SBP estimations and calculated by averaging the results obtained by all three peaks. ^Values in the bracket are the coefficients of the variations. #Values are calculated by the results of the compressive tests. †The name of the specimen is defined as "batch No.–sample No."

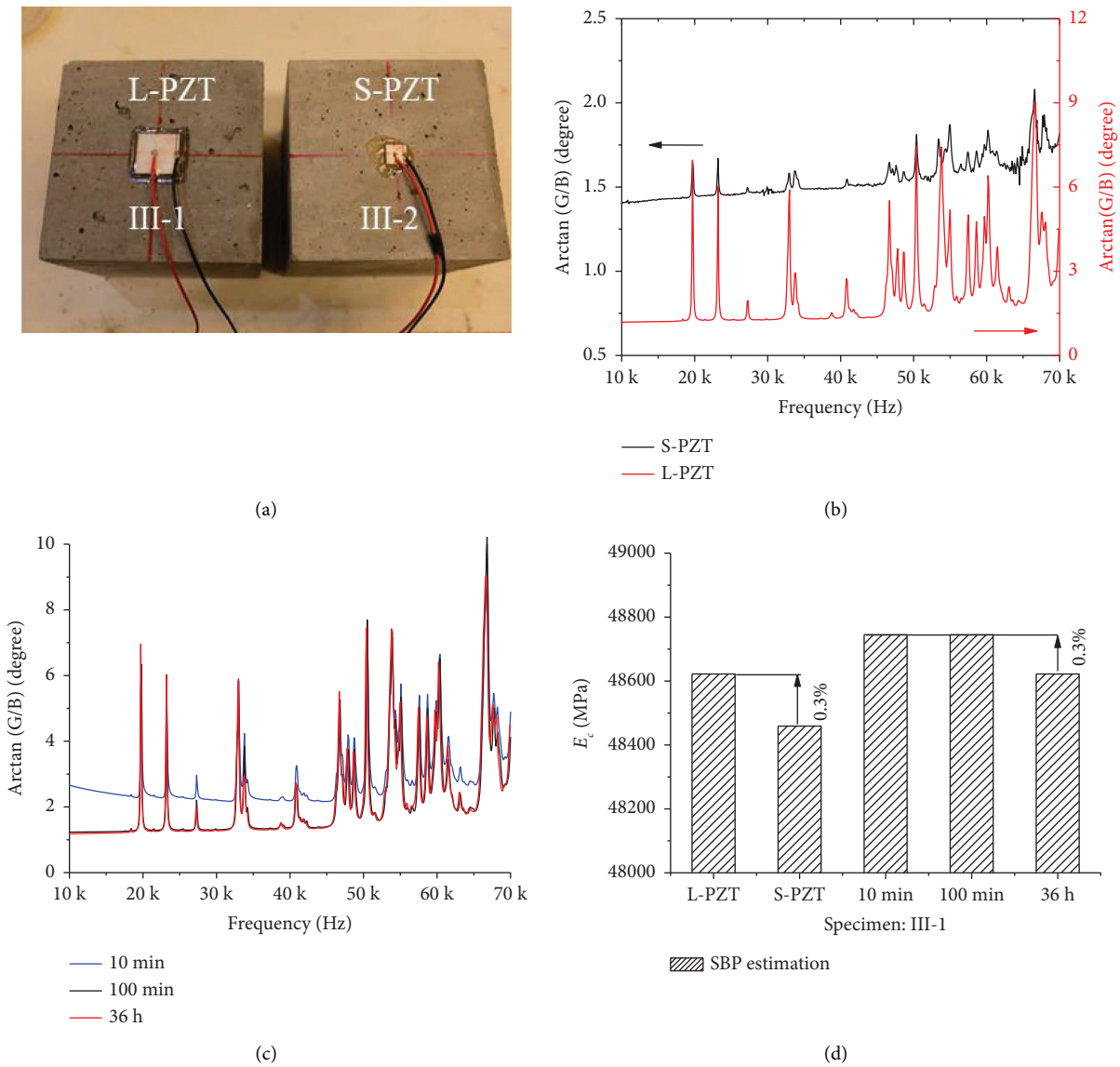

Figure 10: Experimental validation of the repeatability of the signals. (a) Cubes of batch III. (b) PZT size effect (III-1). (c) Effect of hardening of the epoxy (III-1). (d) Comparison in modulus of elasticity.

Figure 10(b) shows the typical signals (specimen III-1) from L-PZT and S-PZT. At 10–70 kHz, both sizes of PZT sensors could capture almost the same frequencies of the selected peaks. This experimental observation confirmed the conclusions obtained in the numerical analyses. The first four peaks were selected to calculate the modulus of

Table 7: Results of repeatability of the indexes.

Specimen	PZT size	Hardening time of epoxy	A/B/C/D (kHz)	E_c (MPa)	Difference
III-1	S-PZT	36 h	19.7/23.2/27.2/32.9	48459	−0.3%
	L-PZT		19.7/23.2/27.3/33.0	48622	—
	L-PZT	10 min	19.8/23.2/27.3/33.0	48745	0.3%
		100 min	19.8/23.2/27.3/33.0	48745	0.3%
		36 h	19.7/23.2/27.3/33.0	48622	—

Note. E_c is calculated by averaging the results obtained based on all four peaks; differences are calculated by comparing them with the status of L-PZT at 36 h.

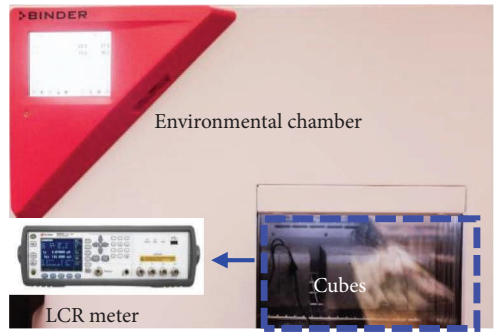

Figure 11: Test setup for temperature effects.

elasticity. As shown in Figure 10(d), the results from L-PZT and S-PZT showed a minimal difference (i.e., −0.3%). Figure 10(b) shows the magnitude of the peaks obtained by the S-PZT patch was smaller than those obtained by the L-PZT patch. For example, peak C recorded by S-PZT was hard to capture, whereas L-PZT can easily identify this peak. The noise level in the S-PZT spectra was close to small peak magnitudes in Figure 10(b), which might present some difficulties in peak selections and misunderstandings in the analyses. According to the experience gained in the experiments, the noise might be attributed to the welding quality, which had more influence on S-PZT. Therefore, large-size PZT patches, which can provide strong and clear signal characteristics for analyses, are recommended for future tests.

The hardening time of the epoxy was another crucial factor in the practical applications of the proposed methods because the hardening time at the measurement moment influences the modulus of elasticity of the epoxy. A quick hardening process is beneficial for capturing the spectra peaks with sufficient repeatability and magnitude as early as possible. The signals recorded by the L-PZT were used to investigate the effect of the hardening time of the adhesive layer. Figure 10(c) plots the recorded signals at 10 min, 100 min, and 36 h after bonding. The increases in the hardening time (from 10 min to 100 min) of the epoxy resulted in the downward shift of the spectra with apparently observed peaks. Given the selected adhesive materials, even the spectrum recorded by L-PZT at 10 min could clearly show those peaks of interest. The spectrum recorded at 36 h showed nearly the same resonant frequencies as the other two sets of data. Among the first four peaks, peaks C and D of the signals recorded at 36 h shifted leftward by 100 Hz, leading to −0.3% differences compared with the other two sets of data, as summarized in Table 7. The difference of E_c between 10 min and 36 h was 0.3%.

The comparisons of the abovementioned two tests are plotted in Figure 10(d). The differences induced by different PZT sensors and different hardening time of bonding were small enough. The largest difference in this specimen was only 163 MPa (i.e., 0.3%), proving that the proposed EMI method can provide repeatable and accurate results.

3.3. Temperature Tests. After the abovementioned tests, the concrete cubes of batch III were tested with the ambient temperature ranging from 5°C to 45°C to validate the effectiveness of this EMI-based method in varying temperature conditions. Figure 11 shows the experimental setup for the temperature tests. The concrete cubes were placed inside an environmental chamber (MKF 115). The measurement was conducted every 20 min after temperature loading was applied. The data collection setup was the same as that described in Section 3.2. Once the RMSD of the arctan (G/B) spectra between every two consecutive measurements was smaller than 0.005, the temperature condition was considered stable.

Considering the conclusion in Section 2.5 shows that the homogenous FEM model may not capture the peaks accurately at a relatively high-frequency range, only the first four cube resonance peaks (peaks A to D) were selected to investigate the temperature effect. Figure 12 shows the experimental results of the temperature effects. The selected peaks shifted leftward with the increasing temperature. Meanwhile, the entire spectra of the signals shifted upward, leading to small magnitudes of the peaks, when the temperature reached 45°C. The same phenomenon could be obtained for all three specimens of batch III as shown in

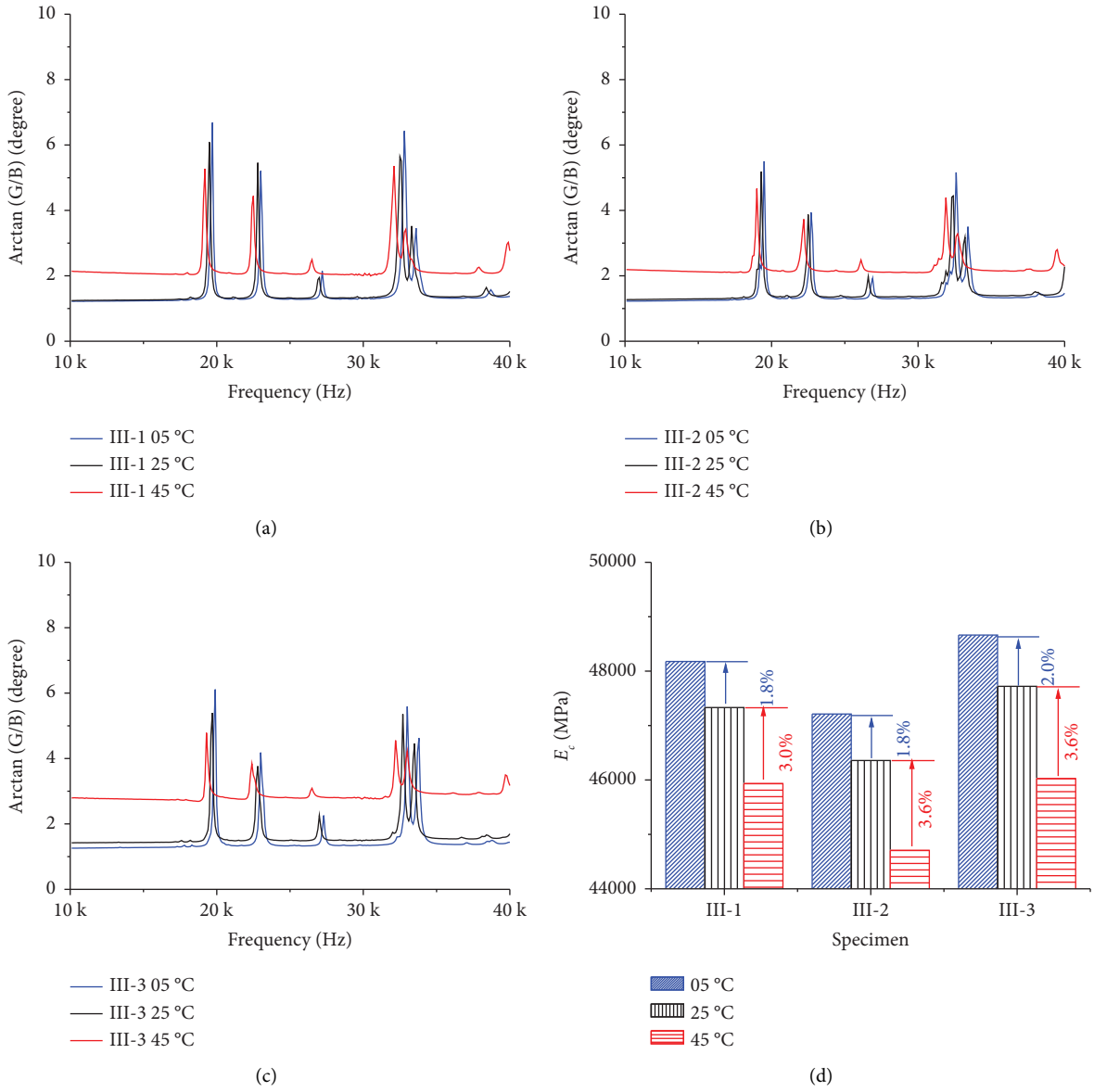

Figure 12: Temperature effects on signals. (a) Experimental results: III-1. (b) Experimental results: III-2. (c) Experimental results: III-3. (d) Comparisons of E_c.

Table 8: Temperature tests on the measurement results.

Specimen	Degree (°C)	A/B/C/D (kHz)	E_c (MPa)	Difference
III-1	05	19.7/23.0/27.2/32.8	48178	1.8%
	25	19.5/22.8/27.0/32.5	47331	—
	45	19.2/22.5/26.5/32.1	45934	−3.0%
III-2	05	19.5/22.7/26.9/32.6	47212	1.8%
	25	19.3/22.5/26.6/32.4	46358	—
	45	19.0/22.0/26.1/31.9	44707	−3.6%
III-3	05	19.9/23.0/27.3/33.0	48662	2.0%
	25	19.7/22.8/27.0/32.7	47721	—
	45	19.3/22.4/26.5/32.2	46026	−3.6%

Note. E_c is calculated by averaging the results obtained by all four peaks; differences are calculated by comparing them with the status of 25°C for each specimen.

Figures 12(a)–12(c). The frequencies of peaks A to D are summarized in Table 8. Elevating the temperature from 25°C to 45°C would lead to larger differences in E_c than elevating the temperature from 5°C to 25°C, as shown in Figure 12(d). Compared with 25°C, the average differences for E_c at 5°C and 45°C were 1.9% and 3.4%, respectively. Notably, the modulus of elasticity of concrete may change by 1.5–6.1% for every 20°C temperature change [39, 40]. Therefore, the proposed method can capture small changes in concrete properties induced by environmental temperature variations. Compared with traditional destructive compressive tests, the proposed method provides an efficient, nondestructive, and *in situ* technique for monitoring the material properties of concrete, helping save human and material costs.

4. Conclusions

A baseline-free EMI resonance method for measuring the modulus of elasticity of concrete was proposed for the first time in this study on the basis of a series of numerical and experimental studies. The repeatable signatures in the proposed arctan (G/B) spectra were identified through the numerical simulations of the standard concrete cubes (100 mm in width) with SBP. Subsequently, a series of experiments were conducted to examine the accuracy and repeatability of the proposed baseline-free EMI resonance method. Some major conclusions are summarized as follows:

(1) The selected cube resonance frequencies can be obtained consistently by different sizes of the PZT patches, indicating that these signature frequencies are highly related to the concrete properties but insensitive to the sizes of PZT patches. Among the studied PZT patches, the PZT patches with large width and thin thickness show the highest sensitivity and thus are recommended in practical applications.

(2) The majority of the selected cube resonance peaks are insensitive to both the adhesive layer thickness and the thermal effects on the sensor system. Given a certain PZT patch, a small thickness of the adhesive layer leads to high sensitivity. It is recommended that the thickness of the adhesive layer should not exceed 0.5 mm, which is easily achievable in practice.

(3) The correlations between the frequencies of the selected cube resonance peaks and $\sqrt{E_c/\rho_c}$ were established numerically. The slopes for the first four peaks were obtained through numerical regression analyses. The experiments on two batches of concrete cubes (SSC and HSC) indicate that the regression formulas can accurately estimate the modulus of elasticity of the concrete cubes.

(4) The repeatability of the signature frequencies obtained by different sizes of patches and the effects of the ambient temperature were validated both numerically and experimentally

(5) The proposed method offers an efficient and nondestructive technique to accurately capture small changes in the modulus of elasticity of concrete

Although this study mainly focuses on measuring the modulus of elasticity of standard concrete cubes that are commonly tested on construction sites, the proposed framework can be extended to assess other material properties (e.g., compressive strength) of concrete cubes or other concrete specimens with different shapes and sizes, which presents a promising research direction in the future.

Data Availability

The numerical and experimental data used to support the findings of this study are included within the article.

Conflicts of Interest

The authors declare that they have no conflicts of interest.

Acknowledgments

The authors gratefully acknowledge the financial support provided by the Research Grants Council of Hong Kong through the theme-based research schemes (Grant nos. T22-502/18-R and T22-501/23-R), the Hong Kong Branch of the National Rail Transit Electrification and Automation Engineering Technology Research Center (Grant no. K-BBY1), and the Joint Research Centre for Marine Infrastructure (Grant no. 1-CEB0).

References

[1] A. M. Neville and J. J. Brooks, *Concrete Technology*, Pearson Education, London, UK, 2nd edition, 2010.

[2] ASTM, *ASTM C39/C39M Standard Test Method for Compressive Strength of Cylindrical concrete Specimens*, American Society for Testing and Materials, West Conshohocken PA, USA, 2020.

[3] ACI (American Concrete Institute), *ACI 318R-19 and ACI 318-19, Building Code Requirements for Structural concrete Commentary*, American Concrete Institute, Michigan, MI, USA, 2019.

[4] H. Gu, G. Song, H. Dhonde, Y. L. Mo, and S. Yan, "Concrete early-age strength monitoring using embedded piezoelectric transducers," *Smart Materials and Structures*, vol. 15, no. 6, pp. 1837–1845, 2006.

[5] R. Bassim and M. Issa, "Dynamic- and static-elastic moduli and strength properties of early-age portland cement concrete pavement mixtures," *Journal of Materials in Civil Engineering*, vol. 32, no. 5, 2020.

[6] W. Li, J. Wang, T. Liu, and M. Luo, "Electromechanical impedance instrumented circular piezoelectric-metal transducer for corrosion monitoring: modeling and validation," *Smart Materials and Structures*, vol. 29, no. 3, Article ID 035008, 2020.

[7] D. Tamhane, J. Thalapil, S. Banerjee, and S. Tallur, "Smart cathodic protection system for real-time quantitative assessment of corrosion of sacrificial anode based on electromechanical impedance (EMI)," *IEEE Access*, vol. 9, pp. 12230–12240, 2021.

[8] Y. Y. Lim, S. T. Smith, and C. K. Soh, "Wave propagation based monitoring of concrete curing using piezoelectric materials: review and path forward," *Non-Destructive Testing and E International*, vol. 99, pp. 50–63, 2018.

[9] C. Liang, F. P. Sun, and C. A. Rogers, "Coupled electro-mechanical analysis of adaptive material systems-determination of the actuator power consumption and system energy transfer," *Journal of Intelligent Material Systems and Structures*, vol. 8, no. 4, pp. 335–343, 1997.
[10] Y. Y. Lim, S. T. Smith, R. V. Padilla, and C. K. Soh, "Monitoring of concrete curing using the electro-mechanical impedance technique: review and path forward," *Structural Health Monitoring*, vol. 20, no. 2, pp. 604–636, 2021.
[11] X. Lu, Y. Y. Lim, and C. K. Soh, "Investigating the performance of "Smart Probe" based indirect EMI technique for strength development monitoring of cementitious materials – modelling and parametric study," *Construction and Building Materials*, vol. 172, pp. 134–152, 2018.
[12] C. K. Soh and S. Bhalla, "Calibration of piezo-impedance transducers for strength prediction and damage assessment of concrete," *Smart Materials and Structures*, vol. 14, no. 4, pp. 671–684, 2005.
[13] Y. F. Su, G. Han, A. Amran, T. Nantung, and N. Lu, "Instantaneous monitoring the early age properties of cementitious materials using PZT-based electro-mechanical impedance (EMI) technique," *Construction and Building Materials*, vol. 225, pp. 340–347, 2019.
[14] S. W. Shin, A. R. Qureshi, J. Lee, and C. B. Yun, "Piezoelectric sensor based nondestructive active monitoring of strength gain in concrete," *Smart Materials and Structures*, vol. 17, no. 5, Article ID 055002, 2008.
[15] S. W. Shin and T. K. Oh, "Application of electro-mechanical impedance sensing technique for online monitoring of strength development in concrete using smart PZT patches," *Construction and Building Materials*, vol. 23, no. 2, pp. 1185–1188, 2009.
[16] J. Kim, C. Lee, S. Park, and K. Koh, "Real-time strength development monitoring for concrete structures using wired and wireless electro-mechanical impedance techniques," *Korean Society of Civil Engineers Journal of Civil Engineering*, vol. 17, no. 6, pp. 1432–1436, 2013.
[17] Y. Yang, Y. Y. Lim, and C. K. Soh, "Practical issues related to the application of the electromechanical impedance technique in the structural health monitoring of civil structures: I. Experiment," *Smart Materials and Structures*, vol. 17, no. 3, Article ID 035008, 2008.
[18] Y. Yang, Y. Y. Lim, and C. K. Soh, "Practical issues related to the application of the electromechanical impedance technique in the structural health monitoring of civil structures: II. Numerical verification," *Smart Materials and Structures*, vol. 17, no. 3, Article ID 035009, 2008.
[19] X. P. Qing, H. Chan, S. J. Beard, T. K. Ooi, and S. A. Marotta, "Effect of adhesive on the performance of piezoelectric elements used to monitor structural health," *International Journal of Adhesion and Adhesives*, vol. 26, no. 8, pp. 622–628, 2006.
[20] G. Li, M. Luo, J. Huang, and W. Li, "Early-age concrete strength monitoring using smart aggregate based on electromechanical impedance and machine learning," *Mechanical Systems and Signal Processing*, vol. 186, no. 8, Article ID 109865, 2023.
[21] V. G. M. Annamdas and Y. Yang, "Practical implementation of piezo-impedance sensors in monitoring of excavation support structures," *Structural Control and Health Monitoring*, vol. 19, no. 2, pp. 231–245, 2012.
[22] T. C. Huynh and J. T. Kim, "RBFN-based temperature compensation method for impedance monitoring in prestressed tendon anchorage," *Structural Control and Health Monitoring*, vol. 25, no. 6, Article ID e2173, 2018.
[23] X. Zhang, W. Zhou, and H. Li, "Electromechanical impedance-based ice detection of stay cables with temperature compensation," *Structural Control and Health Monitoring*, vol. 26, no. 9, 2019.
[24] D. Ai, C. Lin, H. Luo, and H. Zhu, "Temperature effect on electro-mechanical admittance-based concrete structural health monitoring," *Structural Health Monitoring*, vol. 19, no. 3, pp. 661–692, 2020.
[25] Piezo system, "Techniuqe specifications of support documents (America: wildwood Avenue)," 2023, https://support.piezo.com/article/62-material-properties.
[26] Z. S. Tang, Y. Y. Lim, S. T. Smith, and R. V. Padilla, "Modelling of the electromechanical impedance technique for prediction of elastic modulus of structural adhesives," *Structural Health Monitoring*, vol. 20, no. 5, pp. 2245–2260, 2020.
[27] X. Lu, Y. Y. Lim, I. Izadgoshasb, C. K. Soh, and Soh, "Strength development monitoring and dynamic modulus assessment of cementitious materials using EMI-Miniature prism based technique," *Structural Health Monitoring*, vol. 19, no. 2, pp. 373–389, 2020.
[28] Z. Kong and N. Lu, "Improved method to determine Young's modulus for concrete cylinders using electromechanical spectrum: principle and validation," *Journal of Aerospace Engineering*, vol. 19, no. 2, 2020.
[29] S. W. Zhou, C. Liang, and C. A. Rogers, "Integration and design of piezoceramic elements in intelligent structures," *Journal of Intelligent Material Systems and Structures*, vol. 6, no. 6, pp. 733–743, 1995.
[30] A. N. Zagri and V. Giurgiutiu, "Electro-mechanical impedance method for crack detection in thin plates," *Journal of Intelligent Material Systems and Structures*, vol. 12, no. 10, pp. 709–718, 2002.
[31] A. Narayanan, A. Kocherla, and K. V. L. Subramaniam, "Understanding the coupled electromechanical response of a PZT patch attached to concrete: influence of substrate size," *Measurement*, vol. 124, pp. 505–514, 2018.
[32] S. Zhao, S. Fan, J. Yang, and S. Kitipornchai, "Numerical and experimental investigation of electro-mechanical impedance based concrete quantitative damage assessment," *Smart Materials and Structures*, vol. 29, no. 5, Article ID 055025, 2020.
[33] Y. F. Su, G. Han, T. Nantung, and N. Lu, "Novel methodology on direct extraction of the strength information from cementitious materials using piezo-sensor based electromechanical impedance (EMI) method," *Construction and Building Materials*, vol. 259, Article ID 119848, 2020.
[34] R. Georges Sabat, B. K. Mukherjee, W. Ren, and G. Yang, "Temperature dependence of the complete material coefficients matrix of soft and hard doped piezoelectric lead zirconate titanate ceramics," *Journal of Applied Physics*, vol. 101, no. 6, 2007.
[35] S. W. Zhou, C. Liang, and C. A. Rogers, "A dynamic model of piezoelectric actuator-driven thin plates," *Society of Photographic Instrumentation Engineers Proceedings*, vol. 2190, pp. 550–562, 1994.
[36] A. Pauw, "Static modulus of elasticity of concrete as affected by density," *Airports Council International Journal Proceedings*, vol. 57, no. 12, pp. 679–688, 1960.
[37] B. Vakhshouri, "Modulus of elasticity of concrete in design codes and empirical models: analytical study," *Practice*

Periodical on Structural Design and Construction, vol. 23, no. 4, 2018.

[38] S. V. Kolluru, J. S. Popovics, and S. P. Shah, "Determining elastic properties of concrete using vibrational resonance frequencies of standard tests cylinders," *Cement Concrete and Aggregates*, vol. 22, no. 2, pp. 81–89, 2000.

[39] S. N. Shoukry, G. W. William, B. Downie, and M. Y. Riad, "Effect of moisture and temperature on the mechanical properties of concrete," *Construction and Building Materials*, vol. 25, no. 2, pp. 688–696, 2011.

[40] O. Bahr, P. Schaumann, B. Bollen, and J. Bracke, "Young's modulus and Poisson's ratio of concrete at high temperatures: experimental investigations," *Materials and Design*, vol. 45, pp. 421–429, 2013.